Temperature-Driven Dissolution of Nanoalloys During Ink Preparation and Membrane Electrode Assembly Fabrication

Michal Ronovský[1,6], Olivia Dunseath[2], Tomáš Hrbek[3], Peter Kúš[3], Matija Gatalo[4,5], Shlomi Polani[6], Jan Kubt[7], Daniel Götz[7], Hridya Nedumkulam[1,3], Andrea Satori[1], Enrico Petrucco[2], Francisco Ruiz Zepeda[4], Nejc Hodnik[4], Peter Strasser[6], Alex Martinez Bonastre[2], Jakub Drnec[1]*

[1] ESRF—The European Synchrotron, ID 31 Beamline, Grenoble, France
[2] Johnson Matthey Technology Centre, Blount's Court, Sonning Common, Reading RG4 9NH, U.K.
[3] Charles University, Faculty of Mathematics and Physics, Department of Surface and Plasma Science, V Holešovičkách 2, 180 00, Prague 8, Czech Republic
[4] National Institute of Chemistry, Laboratory for Electrocatalysis, Hajdrihova Ulica 19, 1000 Ljubljana, Slovenia
[5] ReCatalyst, Hajdrihova Ulica 19, 1000 Ljubljana, Slovenia
[6] Electrochemical Energy, Catalysis and Material Science Laboratory, Department of Chemistry, Technical University Berlin, Berlin, Germany
[7] Independent researcher
** Corresponding author: Jakub Drnec, email: drnec@esrf.fr*

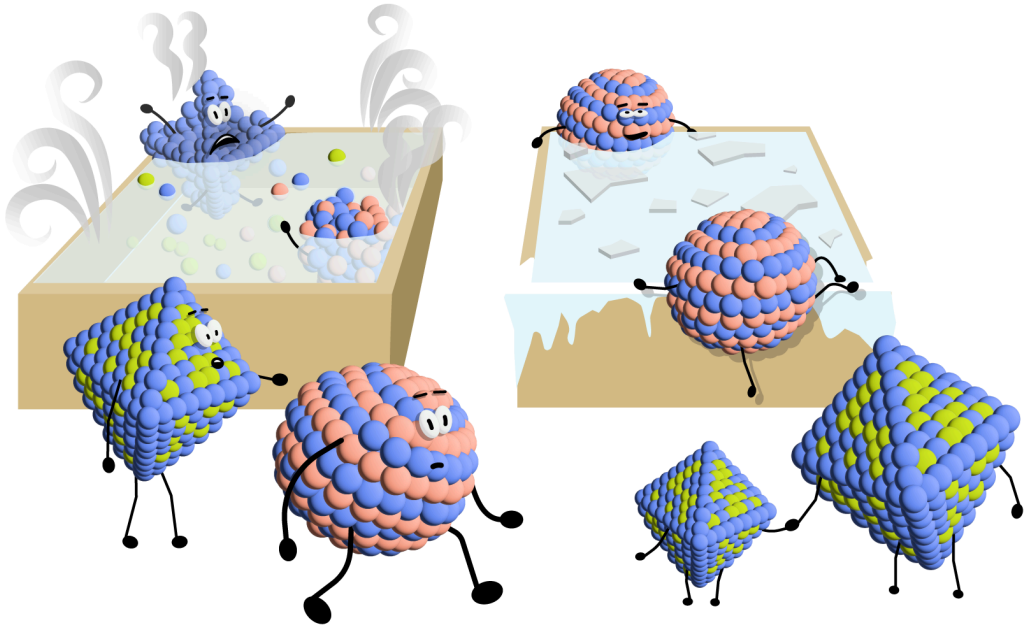

Abstract

Platinum (Pt) alloys are excellent oxygen-reduction catalysts used in proton exchange membrane fuel cells, yet their effective integration poses challenges. Through in-situ X-ray diffraction, we investigate the compositional changes during the ink preparation of PtCo and PtNi catalysts and reveal that dissolution is primarily driven by temperature. Comparisons with conventional catalyst-coated membrane (CCM) fabrication methods highlight structural transformations during hot-pressing. Paving the way for advancements in sustainable energy technologies, our findings emphasize the essential need for fundamental knowledge of ink-making and CCM fabrication to unlock Pt-alloy catalyst potential for hydrogen fuel cells. In addition to the academic community, the industry shall benefit from this precise and easy-to-employ methodology.

Introduction

The ever-increasing need for renewable energy sources drives the development of green technologies based on hydrogen, a clean energy carrier.[1] While proton-exchange membrane fuel cells (PEMFCs) are up to two times more efficient than internal combustion engines,[2] their commercialization is limited by the scarcity of green hydrogen,[3] lack of infrastructure,[4] human skepticism, and the price and durability of the cathode catalyst.[5]

The current state-of-the-art catalysts for the cathodic oxygen reduction reaction (ORR) are platinum (Pt) alloys, particularly those incorporating transition metals (TMs) such as nickel (Ni) and cobalt (Co). Despite their excellent catalytic activity in theory and laboratory experiments,[6] integrating these Pt alloys into membrane electrode assemblies (MEAs) remains a formidable challenge.[7]

In general, MEA-based single-cell activity and catalyst layer stability are tested in both high- and low-current-density regions to mimic the different usage, e.g., driving styles under aggressive acceleration and cruising, respectively.[8] At low current densities (0.9 V vs. RHE), Pt-TM catalysts lose their advantages over Pt/C catalysts during stability testing, and at high current densities (0.67 V vs. RHE) even before the start of an accelerated stress test.[9]

It has been reported that the composition and structure of the as-synthesized powder catalyst changes upon MEA fabrication both for acid[10] and alkaline fuel cells.[11] As a result, the catalytic activity enhancement in MEA is jeopardized as the catalyst itself changes during preparation upon TM dissolution. This is especially the case for shaped-controlled octahedral oh-PtNi alloys where the most ORR active $Pt_3Ni(111)$ facets are the first to dissolve.[12] Moreover, dissolved cations increase mass transport resistance, significantly decreasing performance at high current densities.[13]

There are three main ways to stabilize the Pt-alloy structure against TM dissolution: doping with a third metal (W,[14] Ga,[15] Au, [16] Mo,[17] and/or Rh[18 19]), acid leaching,[20 21 22] and introducing intermetallic superlattice.[23 24 25] Despite substantial efforts in stabilizing Pt alloys and addressing the ramifications of TM dissolution, the ink-making and CCM preparation of Pt alloyed catalysts is overlooked compared to Pt/C catalysts.[26 27] Apart from the pioneering work of D. J. Myers and co-workers,[28] there is a glaring gap in the scientific literature regarding the exploration of Pt-alloy inks.

Here, we show that using conventional methods optimized for Pt/C catalysts, transferring stabilized Pt-alloys to the catalyst-coated membrane (CCM) is very difficult without TM dissolution, altering their composition and structure. Our primary objective is to unravel the intricate relationship between ionomer concentration, temperature, and catalyst dissolution during ink-making using in-situ X-ray diffraction (XRD) (Figure 1a). We compare two common techniques for ink preparation, horn sonication, and ball milling, and assess the structural changes that occur after catalyst layer (CL) deposition and hot-pressing step in CCM fabrication. We show that temperature controls dissolution within the complex ink and MEA environment, demanding the development of different approaches for the efficient incorporation of Pt-alloy catalysts into PEMFCs.

Results

Ink preparation

For a comprehensive perspective, we used several catalysts in the in-situ measurements during horn sonication: octahedral (oh) oh-PtNi(MoRh) stabilized by Mo, oh-PtNi(Ir) [not acid-leached, (XY) denotes doping with a small amount < 3 at% of X and Y metal]; acid-leached 2.7 nm PtCo intermetallics with low (17 wt%) intermetallic phase fraction; acid-leached 4 nm PtCo intermetallics with high (50 wt%) intermetallic fraction; and acid-leached PtCo from Umicore with very high (77 wt%) intermetallic fraction. See also Table 1.

Table 1: Catalyst's parameters used for in-situ ink-making. The crystallite size corresponds to the data fitted with one phase. The intermetallic phase was retrieved using high-resolution ex-situ XRD patterns.

Powder	oh-PtNiMoRh	oh-PtNiIr	2.7 nm PtCo	4 nm PtCo	PtCo Umicore
Ni or Co at%	27.9	16.7	12.7	21.7	19.1
crystallite size (XRD) nm	7.2	7.6	2.7	4	4.5
Intermetallic phase (XRD) wt%	0	0	17	50	77
Pt/C wt%	15.3	17.5	30.3	47.6	27.5
acid-leached	no	no	yes	yes	yes

The in-situ horn sonication setup is composed of a polystyrene cuvette placed into a holder thermally connected to a two-stage Peltier module (Figure 1b) for heating and cooling. A thermocouple and horn sonifier are inserted into the cuvette. The upper part is sealed with Parafilm to prevent evaporation. The sonication is performed in cycles to avoid overheating. Similar to a study on Pt/C catalysts,[29] one cycle comprises of 4 s sonication followed by 8 s thermalization to stabilize the temperature (Figure 1b). X-ray diffractograms (XRD) are acquired in the middle of the thermalization step.

At first, 15 cycles were performed with each catalyst in 1-propanol-water solution for good dispersion. Then, Nafion™ 1100EW ionomer was added to achieve the desired I/C ratio, followed by 300 cycles, equal to 20 min of sonication out of the total experiment time.

The XRD patterns of each cycle were radially integrated, and a lattice parameter was determined using Rietveld refinement to evaluate the kinetics of transition metal dissolution. An example of the lattice parameter evolution for a PtCo catalyst at different temperatures is shown in Figure 1c. The beginning of each curve accounts for thermal equilibration. However, thermal expansion does not fully account for the observed lattice parameter offset, and adsorption processes must be considered as surface adsorption of various species induces bulk strain within nanoparticles.[30] As seen in Figure 1c (colored solid lines), thermal expansion accounts only for 50% and 42% at 52°C and 77°C, respectively. Catalysts reach

thermal and adsorption equilibrium in the first part of the curve, in about 135 cycles (approx. 32 min dashed line). In the second part of the curve, we assume no additional contribution from adsorption takes place, and the lattice parameter change is governed by the dissolution of TM metal, which was calculated according to Vegard's law.[31] The slope of the curve corresponds to the dissolution rate as a loss of TM atomic % per hour. The data analysis is thoroughly described in the SI in the In-situ Rietveld refinement section.

Based on the linearized first-order kinetic model, a higher initial TM amount is expected to lead to faster initial dissolution.[32] Thus, we normalize the dissolution rates by the initial amount of transition metal to get the characteristic dissolution rate constant. These rate constants, plotted in Figure 1d, represent how much each catalyst is prone to dissolution without the initial TM loading bias.

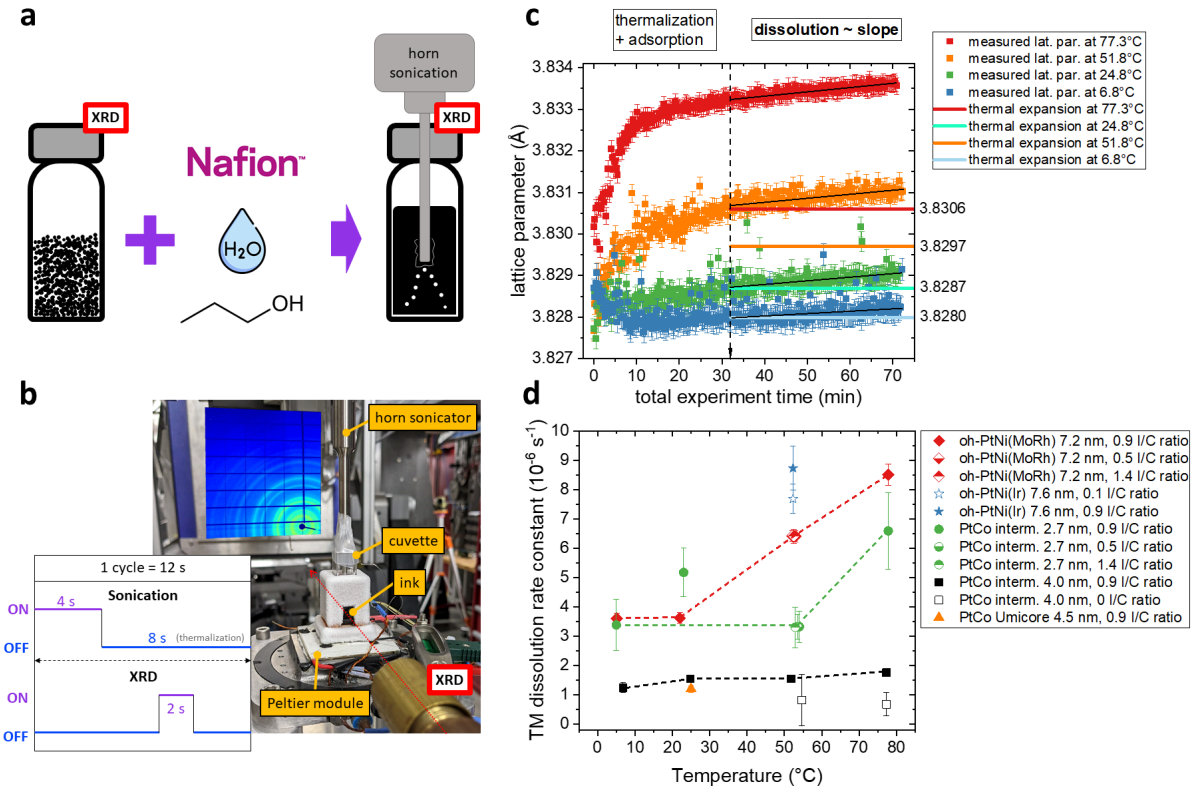

Figure 1: a) A diagram of ink-making: The powder catalyst is horn sonicated with Nafion™ resin, water, and propanol, while its structure and composition are followed by XRD. b) The experimental setup at ID31: A horn sonicator is inserted into a polystyrene cuvette, placed in the copper cuvette holder, and glued to a two-stage Peltier module. The polystyrene cuvette is capped with parafilm to prevent evaporation. The sonication procedure: 4 s of sonication followed by 8 s of thermalization, an XRD pattern is acquired over 2 s in the middle of the thermalization step; c) The evolution of lattice parameter for a PtCo catalyst at different temperatures: The slope in the dissolution region (from 32 min) corresponds to the dissolution according to Vegard's law. d) Dissolution rate constants for the probed catalysts are calculated as the dissolution speed (slope in Figure 1c) divided by the initial alloying amount. Dashed lines are provided as eye guides.

We investigate the influence of two parameters on catalyst dissolution: temperature and Nafion™ concentration. We hypothesize that the highly acidic Nafion™ solution would drive the dissolution, as observed recently.[28] Therefore, we tested I/C ratios from 0 to 1.4. At an

0.9 I/C ratio, the temperature dependence was examined at 5°C, 25°C, 55°C, and 75°C. Contrary to expectations, the octahedral oh-PtNi(MoRh), oh-PtNi(Ir), and 2.7 nm PtCo intermetallic (Figure 1d red, blue, green, respectively) catalysts do not show any dissolution dependence on the I/C ratio in 0.5 to 1.4 range, but clearly, the dissolution increases with temperature for both classes of catalysts. Yet, the dissolution is almost suppressed without the ionomer in the ink solution for the 4 nm PtCo intermetallics (Figure 1d black). Considering that the dissolution rate of the oh-PtNi(Ir) catalyst is the same within the measurement error at 0.1 and 0.9 I/C ratios, we think that the dissolution is driven by the temperature once a rather small specific ionomer concentration covering the whole catalyst's surface is reached. Adding more ionomer solution to the ink leads to a thicker ionomer overlayer but does not contribute to TM dissolution, as seen for concentrations above 0.5 I/C (Figure 1d). This explanation aligns with a previous study showing higher Co dissolution using an ionomer with more sulfonate groups (lower EW).[28] Nevertheless, we show that even the most stable 4 nm PtCo intermetallics undergo slight dissolution at high temperatures with a 0 I/C ratio.

It has been reported that PtCo alloys show a non-monotonic relationship between Co dissolution and particle size, with minimum Co dissolution at 8.1 nm.[33] Therefore, higher stability for 4 nm PtCo intermetallics is expected, as observed here, compared to 2.5 nm PtCo intermetallics. However, the sizes of oh-PtNi(XY) alloys are larger than those of the probed PtCo alloys, yet their TM dissolution rates are higher. We conclude that this discrepancy is due to the acid leaching of all PtCo samples (formation of a Pt-rich shell that slows down dissolution),[34] and their stabilization by the Pt-Co intermetallic structure (lattice ordering). [35] It is supported by the fact that the more intermetallic phase the catalyst has, the less prone is to dissolution, with PtCo Umicore (77 wt% intermetallic phase) showing the least dissolution at 25°C. When comparing the two PtNi-based catalysts, oh-PtNi(MoRh) exhibits a lower dissolution rate than oh-PtNi(Ir) at 55°C. It has been shown that Mo/MoRh doping positively affects structural/compositional stability during thermal annealing under a hydrogen atmosphere,[36] and in rotating-disk electrode experiments.[19] [17] Evidently, the reported stability advantage translates to ink-making. Despite the different nature of tested catalysts, the temperature-driven dissolution seems universal.

MEA fabrication

The next step in MEA preparation is often ink-spraying and hot-pressing. Ideally, it is desired to keep the catalyst in its original state and TM dissolution to a minimum for these subsequent MEA preparation steps. Having elucidated the effect of temperature on the dissolution during sonication ink-making, we compare the changes in compositions throughout standard CCM fabrication using the same XRD analysis ex-situ. The powder of the selected catalysts is first ball-milled for 20 min in a 1-propanol solution with added Nafion™ resin. This ink is sprayed onto PTFE foil to create a catalyst layer (CL), which is then hot-pressed onto a Nafion™ membrane to make the CCM. Crystallite size and TM amounts were estimated from the XRD patterns of the sprayed and hot-pressed CL, as highlighted in the diagram in Figure 2a.

Instead of oh-PtNi(MoRh), here we use oh-PtNi(Mo) with a similar Ni-alloying amount and a similar particle size. Figure 2b and Table 2 show that all of the four selected catalysts, oh-PtNi(Mo), oh-PrNi(Ir), 2.7 nm PtCo intermetallics, and PtCo Umicore, lose TM content in the course of CL preparation, while their crystallite sizes (Figure 2c) increase. Subsequent

hot-pressing increases particle sizes for all the catalysts, but there are separate scenarios for each catalyst with respect to TM content. The oh-PtNi(Mo) loses an additional 2.2 Ni at% CL-to-CCM, totaling 3.2 Ni at% powder-to-CCM. In the case of oh-PtNi(Ir), we observe a surprising increase of 2.1 Ni at% CL-to-CCM. The Co content of 2.7 nm PtCo intermetallics remains the same, while the PtCo Umicore loses 1.4 Co at% in the CL-to-CCM step.

Due to the prominent role of temperature in dissolution, as elucidated in previous paragraphs, it is unsurprising that all catalysts experience additional structural-compositional changes during the spraying and hot-pressing of CL. TEM analysis (Figure S7) supports XRD results. Unlike the rest of the samples, the particle size of oh-PtNiMo reported in Figure 2c should be considered only as an indicative trend. Due to the larger sizes of octahedrons, the Rietveld analysis had to be performed with a fixed smaller microstrain to obtain a reasonable crystallite size. See Supplementary information for more details. In contrast, the lattice parameter is not correlated with any Rietveld-fit parameter and, therefore, is a more reliable parameter to follow. Consequently, the alloying values are determined with 0.06 at% precision on average. The iridium-doped oh-PtNi(Ir) experienced realloying upon hot-pressing. Although surprising, it has been reported that some alloys can undergo realloying under electrochemical conditions, and we suppose that the realloying of oh-PtNiIr could be caused by this catalyst's particular composition and/or morphology.[37] In all cases, dissolved cations adhere to the ionomer within the solution and permeate the membrane once hot-pressed. This is supported by an energy-dispersive X-ray analysis (EDX) of a crack within the sprayed oh-PtNi(Mo) CCM (Figure 2d). The highlighted region of the CCM shows no Pt signal, but Ni is distributed throughout the crack, with the ionomer membrane underneath. Depth analysis with EDX was performed to confirm these conclusions and is reported in the SI. The cations dissolved in the ionomer severely affect the MEA performance by reducing protonic conductivity after critical cationic concentration is reached.[13]

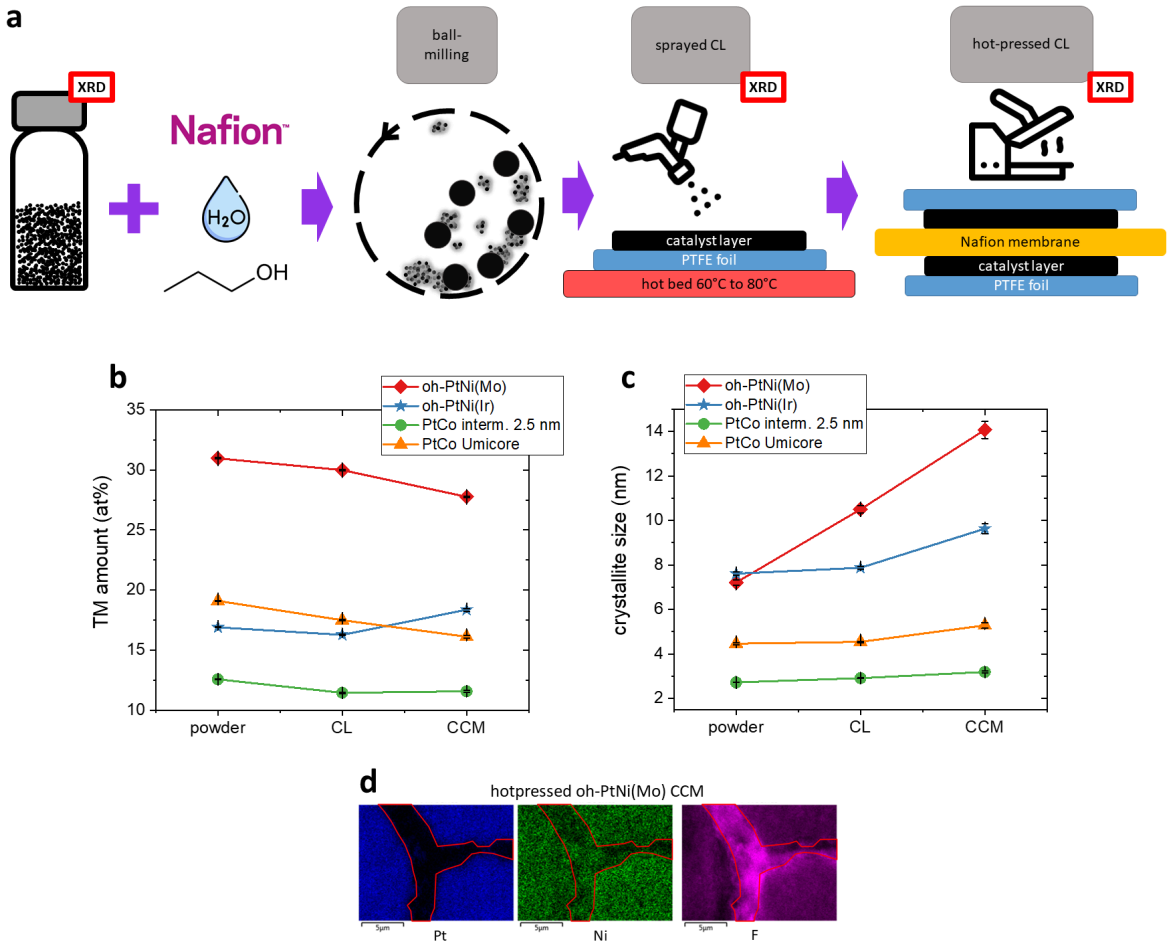

Figure 2: a) Diagram of CCM preparation steps, ex-situ XRD were collected from the sprayed and hot-pressed CL. b) The amount of transition metal and c) crystallite sizes at different stages of CCM preparation determined by ex-situ XRD. Error bars correspond to the Rietveld fit uncertainty. See the ex-situ Rietveld refinement section in SI for more details. d) EDX of a crack within the CL on oh-PtNi(Mo) CCM. Ni diffuses into the membrane upon hot-pressing.

Discussion

The disparity of degradation trends for the four catalysts indicates that the structural-compositional changes experienced during ink-making must depend not only on previously discussed parameters, such as doping and particle size, but also on the mixing method. When comparing TM content lost during ball milling in the powder-to-CL step with the horn sonication, the latter process seems to be milder with a lower dissolved amount of TM (Table 2). As we found that the dissolution during the sonication step is driven mainly by the temperature, we hypothesize the ball-milling procedure is harsher for the catalysts because of the higher temperature in the process. Despite the interrupted ball-milling protocol to prevent overheating the ink, the local temperature at the ball's surfaces where the powder is crushed is unknown and likely higher than the temperature of the ink itself. Given the results above, one could envision a relatively easy solution using a cooled-ball-milling procedure, e.g., with liquid nitrogen,[38] water,[39] air;[40] while avoiding hot-pressing the CL onto the membrane. However, this might not be sufficient as the standard FC operating

temperature is 80°C, which promotes dissolution.[41] Ultimately, anything that does not dissolve during the ink-making/CCM-making procedure will likely dissolve during the FC operation due to the elevated temperature, acidic environment, and operation conditions.[42] [43] [10]

Nevertheless, we suggest avoiding any excess heating of the ink to minimize the amount of transition metal cations within the solution. The stability of suspensions worsens once a certain quantity of ions is present, resulting in the attraction of different carbon particles and forming agglomerates.[44] Printing unstable ink suspension will likely result in cracked catalyst layers with poorer performance. [45]

Table 2: The alloyed metal content and crystallite sizes at different stages of CCM preparation determined by ex-situ XRD. The powder-to-CL TM loss predicted by in-situ horn sonication XRD takes into account 20 min at elevated temperature during CL spraying. See the TM dissolution estimates section in SI for more details.

Sample:	oh-PtNi(Mo)		oh-PtNi(Ir)		PtCo interm. 2.7 nm		PtCo Umicore	
Parameter:	**TM atomic %**	crystallite size (nm)	**TM atomic %**	crystallite size (nm)	**TM atomic %**	crystallite size (nm)	**TM atomic %**	crystallite size (nm)
powder	30.97 ± 0.06	7.2 ± 0.1	16.90 ± 0.04	7.6 ± 0.1	12.57 ± 0.03	2.72 ± 0.01	19.10 ± 0.04	4.46 ± 0.04
CL	29.99 ± 0.05	10.5 ± 0.2	16.27 ± 0.04	7.9 ± 0.1	11.44 ± 0.05	2.91 ± 0.02	17.49 ± 0.06	4.54 ± 0.03
CCM	27.76 ± 0.06	14.07 ± 0.4	18.36 ± 0.11	9.6 ± 0.2	11.57 ± 0.09	3.13 ± 0.04	16.11 ± 0.12	5.28 ± 0.13
powder-to-CL (ball-milled)	-0.98 ± 0.05	+46 %	-0.63 ± 0.04	+3 %	-1.13 ± 0.05	7%	-1.16 ± 0.06	2%
powder-to-CL predicted by in-situ	-0.47 ± 0.01	n.a.	-0.33 ± 0.02	n.a.	-0.14 ± 0.02	n.a.	-0.05 ± 0.01	n.a.
CL-to-CCM	-2.23 ± 0.06	+34 %	+2.09 ± 0.11	+22 %	+0.13 ± 0.08	10%	-1.38 ± 0.12	16%
powder-to-CCM	-3.21 ± 0.06	+95 %	+1.46 ± 0.11	+27 %	-1.00 ± 0.08	17%	-2.99 ± 0.12	18%

Conclusions

In conclusion, we demonstrate the need to carefully optimize current ink-making and CCM fabrication approaches for the optimal incorporation of state-of-the-art Pt alloys into MEAs. Contrary to our expectations, we find that the dissolution of transition metal from the catalyst is mainly driven by temperature and less by the acidity of the ionomer solution within the ink. This phenomenon is universal for all the investigated catalyst types, and it is likely to be

expected in other systems requiring ink preparation and heat treatment to form catalyst layers. Despite the fact that each class of catalysts exhibits slightly different behavior, the largest structural-compositional changes are observed after the catalyst layer is hot-pressed.

Even after many years, the activities of Pt-alloyed catalysts are not fully transferred from laboratories to MEAs. We believe the ink-making process plays a crucial role in this respect and is vastly overlooked. While we acknowledge the scientific effort to create the most active catalyst, it has become clear that unless the catalyst is stable enough to withstand MEA fabrication, its characteristics will not translate into the operating PEMFC. Future investigations of ink preparation using in-situ techniques are necessary to understand the changes that catalysts undergo while going from powder to CCM. Approaches like ours are of interest to the catalysis community and other fields, such as battery materials, where structure and composition changes during materials processing play crucial roles in performance.

Methods

Sample information

PtCo Umicore

Elyst Pt30 0690 catalyst was purchased from Umicore. ICP measurements reported in the datasheet: 27.5 wt% Pt/C loading, Pt:Co [mol/mol] = 2.5.
Powder XRD (ID31) identified 2 phases:

1. PtCo FCC (F m -3 m) non-intermetallic phase: 23 wt%, Pt:Co [mol/mol] = 9.5, with crystallite (particle) size 3.6 nm.
2. PtCo 3/1 P m -3 m intermetallic phase: 77 wt% with crystallite (particle) size 3.6 nm.

As the peak broadening (from the sample parallax) of the intermetallic phase in in-situ ink-making made it impossible to fit more phases reliably, only one PtCo FCC (F m -3 m) phase was fitted to the diffraction patterns to ensure consistency. Powder XRD of this phase showed Pt:Co [mol/mol] = 4.2, with crystallite (particle) size 4.5 nm.

PtCo intermetallics

PtCo intermetallic catalysts were synthesized by ReCatalyst following previously reported processes [46]. Briefly, the electrocatalysts have been prepared in three major steps. In the first step, Pt NPs have been deposited onto carbon support *via* the double passivation galvanic displacement method using a Co/C precursor reported elsewhere.[47] In the second step, the prepared composites with deposited Pt NPs have been thermally annealed to obtain an intermetallic Pt-alloy crystal phase. In the last step, de-alloying (acid washing) was performed in accordance with the work described previously [48].

For 2.7 nm PtCo intermetallics, EDX measurements showed 30.3 wt% Pt/C loading, Pt:Co [mol/mol] = 7.
Powder XRD identified 2 main phases:

1. PtCo FCC (F m -3 m) non-intermetallic phase: 81.3 wt%, Pt:Co [mol/mol] = 9.1, with crystallite size 2.5 nm.
2. PtCo 3/1 P m -3 m intermetallic phase: 17.0 wt%, Pt:Co [mol/mol] = 3, with crystallite size 4.2 nm.

As the peak broadening (from the sample parallax) of the intermetallic phase in in-situ ink-making made it impossible to fit more phases reliably, only the PtCo FCC (F m -3 m) phase was fitted to the diffraction patterns to ensure consistency. Powder XRD of this phase showed Pt:Co [mol/mol] = 7.1, with crystallite size 2.7 nm, thus the sample identification “2.7 nm PtCo intermetallics”.

For 4 nm PtCo intermetallics, EDX showed 47.6 wt% Pt/C loading, Pt:Co [mol/mol] = 3.1. Powder XRD identified 3 phases:

1. PtCo FCC (F m -3 m) non-intermetallic phase: 49 wt%, Pt:Co [mol/mol] = 16.13, with crystallite size 5.2 nm.
2. PtCo 3/1 P m -3 m intermetallic phase: 35.1 wt%, Pt:Co [mol/mol] = 3, with crystallite size 10.3 nm.
3. PtCo P 4/m m m intermetallic phase: 15.8 wt% with crystallite size 13.9 nm.

As the peak broadening (from the sample parallax) of the intermetallic phase in in-situ ink-making made it impossible to fit more phases reliably, only the PtCo FCC (F m -3 m) phase was fitted to the diffraction patterns to ensure consistency. The crystallite size fitted during in-situ ink-making corresponded to 4.0 nm, thus the sample identification “4 nm PtCo intermetallics”. Such a high disparity between crystallite sizes of the two intermetallic phases and the one phase fitted for in-situ ink-making datasets can directly result from sample parallax peak broadening (and convolution) of the original three phases.

oh-PtNi(MoRh), oh-PtNi(Mo), oh-PtNi(Ir)

All the octahedral samples were synthesized using the same protocol, adding different dopant precursors.

Materials

Platinum (II) acetylacetonate ($Pt(acac)_2$, ≥98%) was obtained from Acros, nickel (II) acetylacetonate ($Ni(acac)_2$, ≥98%), rhodium acetylacetonate ($Rh(acac)_3$, 97.0%), iridium acetylacetonate ($Ir(acac)_3$, ≥97%), molybdenum hexacarbonyl ($Mo(CO)_6$, 99.9) were obtained from Sigma Aldrich. Polyvinylpyrrolidone (PVP) (M. W. 10,000) and benzoic acid (99%) were obtained from Alfa Aesar. Benzyl alcohol (BA) (≥99%) was purchased from Carl-Roth, and acetone and ethanol were purchased from VWR International. Carbon black (Vulcan XC -72) was obtained from Cabot Corporation. All chemicals were used as received.

Protocol

For the synthesis of oh-PtNi(Mo)/C nanoparticles, a typical 10:1 scale synthesis was performed (the synthesis protocol was described previously [17]): 0.32 g $Pt(acac)_2$, 0.5 g $Ni(acac)_2$, 0.2 g $Mo(CO)_6$, 3.2 g PVP (10k) and 2 g benzoic acid in 250 mL BA. The 500 mL pressure glass flask was then sealed and placed in a heating mantle for 1 hour with vigorous stirring at 60 ℃. The flask was then heated to 150°C/min with a ramp of 5°C/min. After 12 hours, the reaction solution was allowed to cool to RT. After stirring 0.25 g carbon (Vulcan xc-72R) overnight in 40 ml BA, we added the carbon solution to the reaction solution and

stirred it overnight again. The solution was purified with a mixture of ethanol and acetone in a centrifuge.
For the synthesis of octahedral PtNi(MoRh)/C nanoparticles, we used 0.1 g $Mo(CO)_6$ and added 0.1 g $Rh(acac)_3$.
For the synthesis of octahedral PtNi(Ir)/C nanoparticles, we replaced BA with DMF and $Mo(CO)_6$ with 80 mg $Ir(acac)_3$. We also used 0.25 g $Ni(acac)_2$ and 0.375 g carbon.

Analysis
For oh-PtNi(MoRh), ICP showed 15.3 Pt wt% and Pt:Ni [mol/mol] = 0.5; TEM particle size 10.5 nm; XRD showed Pt:Ni [mol/mol] = 2.6, with crystallite size 7.2 nm.
For oh-PtNi(Mo), no ICP was measured due to the limited amount of the catalyst; nevertheless, XRD showed Pt:Ni [mol/mol] = 2.2, with crystallite size 7.2 nm; the most similar synthesis product to the oh-PtNi(MoRh) available.
For oh-PtNi(Ir), ICP showed 17.5 Pt wt% and Pt:Ni [mol/mol] = 1.1; XRD showed Pt:Ni [mol/mol] = 4.9, with crystallite size 7.6 nm.

In-situ ink sonication

The catalyst powders were weighted into the polystyrene cuvette. A 1-propanol-in-water solvent blend was added, and 15 sonication cycles were performed to achieve good initial dispersion. Then, Nafion™ 1100EW 12.6 wt% aqueous ionomer dispersion was added to achieve the specified I/C ratio. The ink was diluted afterward with deionized water to achieve the targeted ink solids, which varied between 5 to 10 wt%. Consequently, 300 cycles were performed with XRD acquisition. Sonic dismembrator FB-120 with a 1.8” tip was used at 30% amplitude.

Ex-situ ink ball-milling

The cathode catalyst inks were prepared at an ionomer/carbon weight ratio of ca. 0.9/1, using Nafion™ 1100 Equivalent Weight ionomer. The inks were milled at high shear for approximately 20 minutes at suitable high solids before dilution to coating solids and 24 hours of aging.

Catalyst layer preparation

The cathode catalyst layers were prepared by spray coating the inks using a handheld spray gun fed with compressed air onto a PTFE foil placed on a heated vacuum plate with a constant temperature ranging from 60°C to 80°C.

CCM hot-pressing

Catalyst-coated membranes were fabricated using a hot-pressing decal transfer method to combine the cathode catalyst layer, Nafion™ 112 membrane, and anode catalyst layer (Commercial Johnson Matthey catalyst (HiSPEC™ 3000– 20wt%Pt/C at ca 0.1 $mg_{Pt}\,cm^{-2}$ loading).

X-ray diffraction

X-ray diffraction (XRD) data were collected at the ID31 beamline at the European Synchrotron Radiation Facility. A 2D Pilatus 2M CdTe detector was used at a distance of 0.95 m from the sample. The photon wavelength was 0.161 Å (77.00 keV), just below the Pt K-edge. The beam size was approximately 0.5 mm × 0.5 mm (vertical x horizontal) with a flux of 10^{13} photons/s. The exposure time was 2 s per cycle and 1 s per ex-situ sample. High-resolution ex-situ powder diffractograms were acquired from a small amount of powder catalyst in a Kapton® capillary with a 1 mm diameter. Raw diffraction patterns were radially integrated using PyFAI.[49] Integrated 1D powder diffractograms were loaded into GSAS-II, and sequential Rietveld analysis was performed to extract lattice parameters and crystallite sizes.[50]

Acknowledgments

This project has received funding from the European Union's Horizon 2020 research and innovation program under the Marie Skłodowska-Curie grant agreement No 847439.
We acknowledge ESRF for enabling and supporting this research. Stored data can be obtained upon request. We thank Helena Isern and Florian Russello for their help with the ID31 beamline setup.
We acknowledge the Partnership for Soft Condensed Matter (PSCM) for providing the horn sonicator and the ESRF Sample Environment group for providing the two-stage Peltier module.
We acknowledge Dr. Martha Briceno de Gutierrez and Dr. Emily Brooke of the Johnson Matthey Technology Centre Advanced Characterisation Team for their expertise and for providing FIB-SEM-EDX images of catalyst materials.
We acknowledge the Slovenian Research And Innovation Agency (ARIS) programs P2–0393 and I0–0003 and projects N2-0257 and J7-4637. We also acknowledge EIC Transition project ENABLER (Grant agreement ID: 101112991), European Research Council (ERC) Starting Grant 123STABLE (Grant agreement ID: 852208), and Proof of Concept Grant StableCat (Grant agreement ID: 966654).
Figures include icons designed using images from Flaticon.com.

Bibliography

1. Pivovar, B., Rustagi, N. & Satyapal, S. Hydrogen at Scale (H2@Scale): Key to a Clean, Economic, and Sustainable Energy System. *Electrochem. Soc. Interface* **27**, 47 (2018).
2. Haseli, Y. Maximum conversion efficiency of hydrogen fuel cells. *Int. J. Hydrogen Energy* **43**, 9015–9021 (2018).
3. Kakoulaki, G. *et al.* Green hydrogen in Europe – A regional assessment: Substituting existing production with electrolysis powered by renewables. *Energy Convers. Manage.* **228**, 113649 (2021).

4. IRENA. *Hydrogen: A renewable energy perspective*. (International Renewable Energy Agency, 2019).
5. Wang, Y.-J. *et al.* Unlocking the door to highly active ORR catalysts for PEMFC applications: polyhedron-engineered Pt-based nanocrystals. *Energy Environ. Sci.* **11**, 258–275 (2018).
6. Wang, X. *et al.* Review of Metal Catalysts for Oxygen Reduction Reaction: From Nanoscale Engineering to Atomic Design. *Chem* **5**, 1486–1511 (2019).
7. Pan, L., Ott, S., Dionigi, F. & Strasser, P. Current challenges related to the deployment of shape-controlled Pt alloy oxygen reduction reaction nanocatalysts into low Pt-loaded cathode layers of proton exchange membrane fuel cells. *Current Opinion in Electrochemistry* **18**, 61–71 (2019).
8. Cullen, D. A. *et al.* New roads and challenges for fuel cells in heavy-duty transportation. *Nature Energy* **6**, 462–474 (2021).
9. Wang, X., Hu, L., Neyerlin, K. C. & Ahluwalia, R. K. Baselining Activity and Stability of ORR Catalysts and Electrodes for Proton Exchange Membrane Fuel Cells for Heavy-Duty Applications. *J. Electrochem. Soc.* **170**, 024503 (2023).
10. Ronovsky, M. *et al.* Assessing Utilization Boundaries for Pt-Based Catalysts in an Operating Proton-Exchange Membrane Fuel Cell. *ACS Appl. Energy Mater.* **6**, 8660–8665 (2023).
11. Saveleva, V. A. *et al.* Fe–N–C Electrocatalyst and Its Electrode: Are We Talking about the Same Material? *ACS Appl. Energy Mater.* **6**, 611–616 (2023).
12. Gan, L. *et al.* Element-specific anisotropic growth of shaped platinum alloy nanocrystals. *Science* **346**, 1502–1506 (2014).
13. Lee, C. *et al.* Toward a Comprehensive Understanding of Cation Effects in Proton Exchange Membrane Fuel Cells. *ACS Appl. Mater. Interfaces* **14**, 35555–35568 (2022).
14. Liang, J. *et al.* Tungsten-Doped L10 -PtCo Ultrasmall Nanoparticles as a High-Performance Fuel Cell Cathode. *Angew. Chem. Int. Ed Engl.* **58**, 15471–15477 (2019).

15. Lim, J. *et al.* Ga-Doped Pt-Ni Octahedral Nanoparticles as a Highly Active and Durable Electrocatalyst for Oxygen Reduction Reaction. *Nano Lett.* **18**, 2450–2458 (2018).
16. Lu, B.-A. *et al.* Octahedral PtCu alloy nanocrystals with high performance for oxygen reduction reaction and their enhanced stability by trace Au. *Nano Energy* **33**, 65–71 (2017).
17. Polani, S. *et al.* Highly Active and Stable Large Mo-Doped Pt-Ni Octahedral Catalysts for ORR: Synthesis, Post-treatments, and Electrochemical Performance and Stability. *ACS Appl. Mater. Interfaces* **14**, 29690–29702 (2022).
18. Beermann, V. *et al.* Rh-Doped Pt-Ni Octahedral Nanoparticles: Understanding the Correlation between Elemental Distribution, Oxygen Reduction Reaction, and Shape Stability. *Nano Lett.* **16**, 1719–1725 (2016).
19. Hornberger, E. *et al.* On the electrocatalytical oxygen reduction reaction activity and stability of quaternary RhMo-doped PtNi/C octahedral nanocrystals. *Chem. Sci.* **13**, 9295–9304 (2022).
20. Han, B. *et al.* Record activity and stability of dealloyed bimetallic catalysts for proton exchange membrane fuel cells. *Energy Environ. Sci.* **8**, 258–266 (2014).
21. Ahluwalia, R. K. *et al.* Durability of DE-alloyed platinum-nickel cathode catalyst in low platinum loading membrane-electrode assemblies subjected to accelerated stress tests. *J. Electrochem. Soc.* **165**, F3316–F3327 (2018).
22. Chiwata, M. *et al.* Oxygen Reduction Reaction Activity of Carbon-Supported Pt-Fe, Pt-Co, and Pt-Ni Alloys with Stabilized Pt-Skin Layers. *Electrochemistry* **84**, 133–137 (2016).
23. Wang, J. *et al.* Pt-Based Intermetallic Compound Catalysts for the Oxygen Reduction Reaction: Structural Control at the Atomic Scale to Achieve a Win–Win Situation Between Catalytic Activity and Stability. *Electrochemical Energy Reviews* **6**, 6 (2023).
24. Xiao, W., Lei, W., Gong, M., Xin, H. L. & Wang, D. Recent Advances of Structurally Ordered Intermetallic Nanoparticles for Electrocatalysis. *ACS Catal.* **8**, 3237–3256 (2018).

25. Li, J. *et al.* Hard-Magnet L10-CoPt Nanoparticles Advance Fuel Cell Catalysis. *Joule* **3**, 124–135 (2019).
26. Pollet, B. G. & Goh, J. T. E. The importance of ultrasonic parameters in the preparation of fuel cell catalyst inks. *Electrochim. Acta* **128**, 292–303 (2014).
27. Mo, S. *et al.* Recent Advances on PEM Fuel Cells: From Key Materials to Membrane Electrode Assembly. *Electrochemical Energy Reviews* **6**, 28 (2023).
28. Myers, D. J. *et al.* Degradation of platinum-cobalt alloy PEMFC cathode catalysts in catalyst-ionomer inks. *J. Electrochem. Soc.* **168**, 044510 (2021).
29. Wang, M. *et al.* Impact of catalyst ink dispersing methodology on fuel cell performance using in-situ X-ray scattering. *ACS Appl. Energy Mater.* **2**, 6417–6427 (2019).
30. Chattot, R. *et al.* Electrochemical Strain Dynamics in Noble Metal Nanocatalysts. *J. Am. Chem. Soc.* **143**, 17068–17078 (2021).
31. Denton, A. R. & Ashcroft, N. W. Vegard's law. *Phys. Rev. A* **43**, 3161–3164 (1991).
32. Skrdla, P. J. A simple model for complex dissolution kinetics: a case study of norfloxacin. *J. Pharm. Biomed. Anal.* **45**, 251–256 (2007).
33. Wang, X. *et al.* Effect of Particle Size on the Dissolution of Pt3Co/C and Pt/C PEMFC Electrocatalysts. *J. Electrochem. Soc.* **168**, 054516 (2021).
34. Sasaki, K. *et al.* Core-protected platinum monolayer shell high-stability electrocatalysts for fuel-cell cathodes. *Angew. Chem. Int. Ed Engl.* **49**, 8602–8607 (2010).
35. Cui, Y. *et al.* Mitigating Metal Dissolution and Redeposition of Pt-Co Catalysts in PEM Fuel Cells: Impacts of Structural Ordering and Particle Size. *J. Electrochem. Soc.* **167**, 064520 (2020).
36. MacArthur, K. E. *et al.* Post-Synthesis Heat Treatment of Doped PtNi-Alloy Fuel-Cell Catalyst Nanoparticles Studied by In-Situ Electron Microscopy. *ACS Appl. Energy Mater.* **6**, 5959–5967 (2023).
37. Wu, Z.-P. *et al.* Alloying-realloying enabled high durability for Pt-Pd-3d-transition metal nanoparticle fuel cell catalysts. *Nat. Commun.* **12**, 859 (2021).
38. Cryomill - the perfect mill for cryogenic grinding - RETSCH.

https://www.retsch.com/products/milling/ball-mills/mixer-mill-cryomill/.

39. Kwon, Y.-S., Gerasimov, K. B. & Yoon, S.-K. Ball temperatures during mechanical alloying in planetary mills. *J. Alloys Compd.* **346**, 276–281 (2002).
40. He, S. *et al.* Effect of ball-milling on the physicochemical properties of maize starch. *Biotechnol Rep (Amst)* **3**, 54–59 (2014).
41. Dubau, L. & Maillard, F. Unveiling the crucial role of temperature on the stability of oxygen reduction reaction electrocatalysts. *Electrochem. commun.* **63**, 65–69 (2016).
42. Đukić, T. *et al.* Understanding the Crucial Significance of the Temperature and Potential Window on the Stability of Carbon Supported Pt-Alloy Nanoparticles as Oxygen Reduction Reaction Electrocatalysts. *ACS Catal.* **12**, 101–115 (2022).
43. Chattot, R. *et al.* Break-In Bad: On the Conditioning of Fuel Cell Nanoalloy Catalysts. *ACS Catal.* **12**, 15675–15685 (2022).
44. Baez-Cotto, C. M. *et al.* Impact of polymer additives on crack mitigation of rod-coated fuel cell cathode catalyst layers. *J. Power Sources* **592**, 233852 (2024).
45. Khedekar, K. *et al.* Revealing in-plane movement of platinum in polymer electrolyte fuel cells after heavy-duty vehicle lifetime. *Nature Catalysis* **6**, 676–686 (2023).
46. Pavko, L. *et al.* Toward the Continuous Production of Multigram Quantities of Highly Uniform Supported Metallic Nanoparticles and Their Application for Synthesis of Superior Intermetallic Pt-Alloy ORR Electrocatalysts. *ACS Appl Energy Mater* **4**, 13819–13829 (2021).
47. Gatalo, M. *et al.* A Double-Passivation Water-Based Galvanic Displacement Method for Reproducible Gram-Scale Production of High-Performance Platinum-Alloy Electrocatalysts. *Angew. Chem. Int. Ed Engl.* **58**, 13266–13270 (2019).
48. Gatalo, M. *et al.* Importance of Chemical Activation and the Effect of Low Operation Voltage on the Performance of Pt-Alloy Fuel Cell Electrocatalysts. *ACS Appl Energy Mater* **5**, 8862–8877 (2022).
49. Kieffer, J. & Wright, J. P. PyFAI: a Python library for high performance azimuthal integration on GPU. *Powder Diffr.* **28**, S339–S350 (2013).

50. Toby, B. H. & Von Dreele, R. B. GSAS-II: the genesis of a modern open-source all purpose crystallography software package. *J. Appl. Crystallogr.* **46**, 544–549 (2013).